MATERIALS SCIENCE

10.1126/sciadv.1501459

Edge-selenated graphene nanoplatelets as durable metal-free catalysts for iodine reduction reaction in dye-sensitized solar cells

Myung Jong Ju,[1]* In-Yup Jeon,[1]* Hong Mo Kim,[2]* Ji Il Choi,[3]* Sun-Min Jung,[1] Jeong-Min Seo,[1] In Taek Choi,[2] Sung Ho Kang,[2] Han Seul Kim,[3] Min Jong Noh,[3] Jae-Joon Lee,[4] Hu Young Jeong,[5] Hwan Kyu Kim,[2†] Yong-Hoon Kim,[3†] Jong-Beom Baek[1†]

Metal-free carbon-based electrocatalysts for dye-sensitized solar cells (DSSCs) are sufficiently active in Co(II)/Co(III) electrolytes but are not satisfactory in the most commonly used iodide/triiodide (I^-/I_3^-) electrolytes. Thus, developing active and stable metal-free electrocatalysts in both electrolytes is one of the most important issues in DSSC research. We report the synthesis of edge-selenated graphene nanoplatelets (SeGnPs) prepared by a simple mechanochemical reaction between graphite and selenium (Se) powders, and their application to the counter electrode (CE) for DSSCs in both I^-/I_3^- and Co(II)/Co(III) electrolytes. The edge-selective doping and the preservation of the pristine graphene basal plane in the SeGnPs were confirmed by various analytical techniques, including atomic-resolution transmission electron microscopy. Tested as the DSSC CE in both $Co(bpy)_3^{2+/3+}$ (bpy = 2,2′-bipyridine) and I^-/I_3^- electrolytes, the SeGnP-CEs exhibited outstanding electrocatalytic performance with ultimately high stability. The SeGnP-CE–based DSSCs displayed a higher photovoltaic performance than did the Pt-CE–based DSSCs in both SM315 sensitizer with $Co(bpy)_3^{2+/3+}$ and N719 sensitizer with I^-/I_3^- electrolytes. Furthermore, the I_3^- reduction mechanism, which has not been fully understood in carbon-based CE materials to date, was clarified by an electrochemical kinetics study combined with density functional theory and nonequilibrium Green's function calculations.

INTRODUCTION

Key components of a dye-sensitized solar cell (DSSC) are dye-coated titanium dioxide (TiO_2) as photoanode, electrolyte, and counter electrode (CE). The most common electrolytes and CE are iodide/triiodide (I^-/I_3^-) and an optically transparent film of platinum (Pt) nanoparticles on F-doped SnO_2 (Pt-FTO), respectively (*1*). Although Pt-based materials have long been considered one of the most efficient CEs, Pt is a high-cost precious metal with limited supply. Because of this, alternative materials to Pt have been actively sought after, and among the strongest candidates are carbon-based materials, such as carbon nanotubes (*2*, *3*), porous carbon (*4*–*6*), carbon spheres (*7*), active carbon (*8*), and graphene (*9*–*16*), as well as conducting polymers (*17*) and inorganic materials (*18*, *19*). Specifically, carbon-based materials are the second most widely studied materials for DSSC CEs after Pt because of their good electrocatalytic activity together with stability and low cost. Carbon-based CEs in Co(II)/Co(III) electrolytes have demonstrated high power conversion efficiency (PCE) (*9*–*13*). However, they are not sufficiently active in I^-/I_3^- (*14*, *15*), which are more common and desirable electrolytes for efficient reaction kinetics. Moreover, in terms of overcoming the challenge, the I_3^- reduction mechanism on the carbon-based CE/electrolyte interface has not been fully understood either.

Here, we report edge-selenated graphene nanoplatelets (SeGnPs) as a CE material that works in both $Co(bpy)_3^{2+/3+}$ (bpy = 2,2′-bipyridine) and I^-/I_3^- electrolytes. The overall PCE and electrocatalytic performances are superior to those of Pt-CEs in both electrolytes. The origin of the superiority of SeGnPs as the CE materials for $Co(bpy)_3^{3+}$ and I_3^- reduction reactions was investigated by electrochemical kinetics, density functional theory (DFT), and nonequilibrium Green's function (NEGF) calculations. These new findings may pave the way for further development of more practical Pt-free CEs, which may help to accelerate the practical applications of DSSCs.

RESULTS

Synthesis and characterization of SeGnPs

SeGnPs were prepared by mechanochemical reaction between graphite and selenium (Se) powders (fig. S1). The mechanochemical reaction is driven by kinetic energy (*20*). For example, high-velocity stainless steel balls in a planetary ball mill reactor generate sufficient kinetic energy, which is delivered to graphite and Se powders and induces unzipping of graphitic C–C bonds and cracking of Se–Se bonds (fig. S1). Activated C and Se atoms have an opportunity to form covalent C═Se and C–Se–C bonds (as like C═O and C–O–C bonds) along the broken edges of SeGnPs. The resultant SeGnPs were characterized by various techniques including scanning electron microscopy (SEM; fig. S2) and transmission electron microscopy (TEM; Fig. 1 and fig. S3) with element mappings, energy-dispersive spectroscopy (EDS; fig. S4A and table S1), x-ray photoelectron spectroscopy (XPS; fig. S4, B to D and F), Brunauer-Emmett-Teller (BET) measurements (fig. S5A), Raman spectroscopy (fig. S5B), x-ray diffraction (XRD) patterns (fig. S5C), contact

[1]School of Energy and Chemical Engineering, Center for Dimension-Controllable Organic Frameworks, Ulsan National Institute of Science and Technology (UNIST), 50, UNIST, Ulsan 689-798, Korea. [2]Global GET-Future Laboratory and Department of Advanced Materials Chemistry, Korea University, 2511 Sejong-ro, Sejong 339-700, Korea. [3]Graduate School of Energy, Environment, Water, and Sustainability, Korea Advanced Institute of Science and Technology, 291 Daehak-ro, Daejeon 305-701, Korea. [4]Department of Energy and Materials Engineering, Dongguk University, 30 Pildong-ro 1-gil, Junggu, Seoul 04620, Korea. [5]UNIST Central Research Facilities (UCRF), 50, UNIST, Ulsan 689-798, Korea.
*These authors contributed equally to this work.
†Corresponding author. Email: jbbaek@unist.ac.kr (J.-B.B.); y.h.kim@kaist.ac.kr (Y.-H.K.); hkk777@korea.ac.kr (H.K.K.)

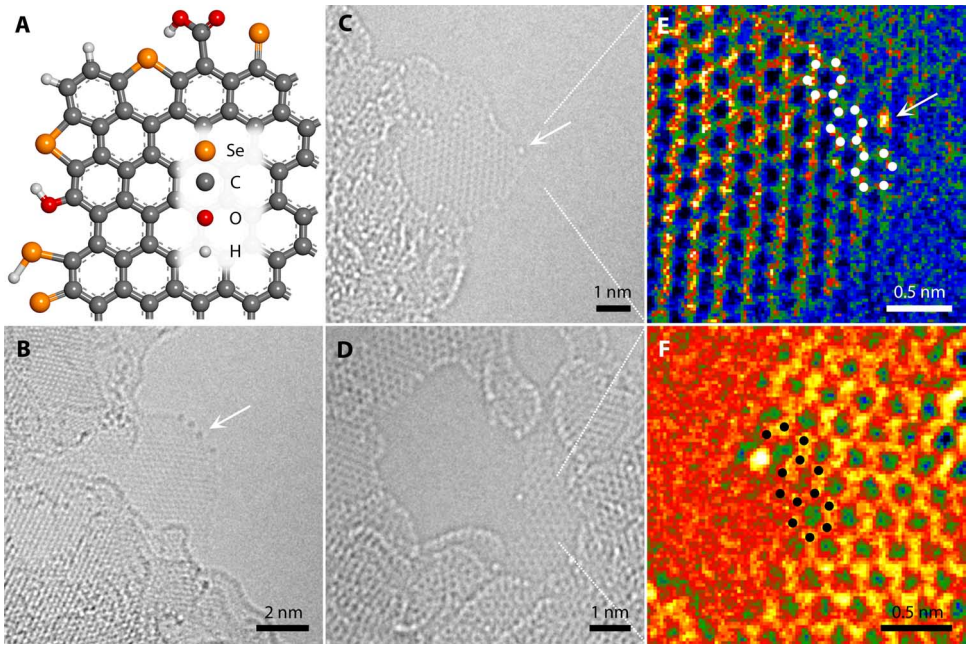

Fig. 1. Structural identification of SeGnPs. (**A**) Proposed atomic model of SeGnPs. (**B**) AR-TEM image obtained at the edge of SeGnPs. (**C** and **D**) Magnified AR-TEM images. (**E** and **F**) Corresponding inverse fast Fourier transform (IFFT) images of a graphene edge with armchair and zigzag configurations, respectively.

angle measurements (fig. S5D), thermogravimetric analyses (fig. S6), and solubility tests (fig. S7). SEM-EDS indicated that the content of Se is approximately 5.57 atomic % (table S1). More detailed characterization data with corresponding discussions are presented in the Supplementary Materials. In particular, the formation of C=Se and C–Se–C bonds at the edges of SeGnPs was demonstrated by a low-voltage spherical aberration (Cs)–corrected atomic-resolution TEM (AR-TEM; Fig. 1B and fig. S8A), high-resolution TEM (HR-TEM; fig. S8B), and scanning TEM (STEM; fig. S8, C and D). The AR-TEM images obtained at the edges of a thin platelet demonstrated in Fig. 1B and fig. S8A show that the Se atoms with the dark atomic contrast are present only along the edge lines of SeGnPs. In contrast, the inner part (basal area) of the sheets shows a perfect graphitic structure, indicating that the mechanochemical unzipping of graphitic C–C bonds does not destroy the crystallinity of the basal plane. A high-angle annular dark-field STEM image (fig. S8, C and D) with atomic *Z* contrast shows the existence of single Se atoms (arrow, bright spots) but not Se clusters. AR-TEM images (arrows, bright atomic contrast of Fig. 1, C and D) and corresponding IFFT images (bright atomic contrast of Fig. 1, E and F) confirm that the single Se atoms are attached at the edge of the armchair or zigzag configurations of graphene, which agrees with our model of edge-selective formation of C–Se bonds, proposed in Fig. 1A.

Electrocatalytic activity of SeGnPs

Given the identification of structure and properties, the electrocatalytic activities of SeGnPs were evaluated for use as CEs in DSSCs. The formation of SeGnP thin films (fig. S9) and fabrication of DSSCs are described in the Supplementary Materials. Electrocatalytic activity was tested with a symmetrical dummy cell by using two identical electrodes through the electrochemical impedance spectroscopy (EIS) technique (fig. S10A). The EIS spectra obtained from $Co(bpy)_3^{2+/3+}$ and I^-/I_3^- electrolytes are shown in Fig. 2 (A and B). Regardless of the electrodes, the EIS spectra for $Co(bpy)_3^{2+/3+}$ electrolyte exhibited two distinct semicircles in high- and low-frequency regions, and they were fitted to the Randles-type equivalent circuit (EC; fig. S10B) (*21*). The corresponding EIS parameters are summarized in Table 1. The SeGnPs exhibited profoundly better electrocatalytic activity than those of the reference Pt and edge-hydrogenated GnPs (HGnPs) (fig. S11). For example, the charge-transfer resistances (R_{ct}'s) of the Pt-CEs and SeGnP-CEs were 1.85 and 0.14 ohms·cm^2, respectively, with corresponding exchange current densities (J_0's) of 13.9 and 234 mA cm^{-2}.

Unlike the Pt with two semicircles, for which the high- and low-frequency semicircles correspond to the charge-transfer and Nernst diffusion processes (Fig. 2B), respectively (*21*, *22*), the EIS spectra of SeGnPs (Fig. 2B) and HGnPs (fig. S12) in I^-/I_3^- electrolytes exhibit three semicircles, which is a general feature of highly porous carbon materials (*6*, *13*, *23*, *24*). Comparing the SeGnP and HGnP electrodes, there is only a slight difference in the magnitude of the first semicircles, but there is a considerable difference in the second semicircles. In this case, the effective charge-transfer resistance ($\mathfrak{R}_{ct}$) should be considered, and several ECs have been proposed to identify and quantify these effects (fig. S13) (*14*, *23*, *24*). For the first semicircle newly emerging in the carbon-based CEs, several proposals have been made as to its origin, including Nernst diffusion in the pores; however, some issues still remain. For example, several of our results conflict with the first semicircle arising from any type of Nernst diffusion in the pores: (i) there was no line of slope 1 (the Warburg line) at the beginning of the semicircle (Fig. 2B); (ii) the semicircles were not enlarged by increasing the electrode thickness (fig. S14, D and E), electrolyte viscosity (fig. S14F), or external bias potential (fig. S15); and (iii) the pore size of the SeGnPs was 26 Å (table S2), which is considerably larger than that of I_3^- and $Co(bpy)_3^{3+}$ ions (table S3). Considering the size difference between I_3^- and $Co(bpy)_3^{3+}$, apparently, the first semicircle that appeared at a high

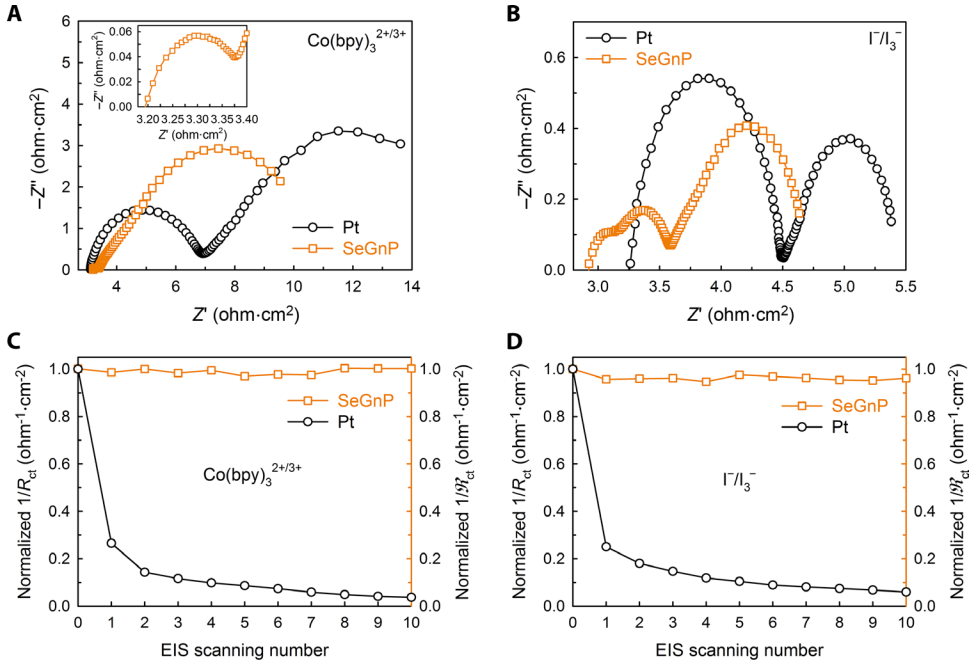

Fig. 2. Comparison between conventional Pt and SeGnP electrodes. (**A** and **B**) Nyquist plots of the Pt-CEs and SeGnP-CEs: $Co(bpy)_3^{2+/3+}$ (A) and I^-/I_3^- (B). The inset in (A) is an enlargement of the EIS spectrum of the SeGnP-CEs in high-frequency range. (**C** and **D**) Normalized R_{ct} and $\mathscr{H}_{ct}$ changes versus the EIS scan number: $Co(bpy)_3^{2+/3+}$ (C) and I^-/I_3^- (D).

Table 1. EIS parameters of symmetrical dummy cells with Pt and SeGnP electrodes. R_s, serial resistance; R_{ct}, charge-transfer resistance; C_{dl}, double-layer capacitance; R_{tm}, transmission resistance; C_{ad}, capacitance due to the adsorption of I^-/I_3^- on the graphitic basal plane; J_0, exchange current density.

CE	Electrolyte	R_s (ohm·cm^2)	R_{ct} (ohm·cm^2)	C_{dl} (μF cm^2)	R_{tm} (ohm·cm^2)	C_{ad} (μF cm^2)	J_0 (mA cm^{-2})
Pt	$Co(bpy)_3^{2+/3+}$	3.12	1.85	8.88	—	—	13.9
SeGnPs		3.20	0.13	17.5	—	—	234
Pt	I^-/I_3^-	3.42	0.61	6.02	—	—	21.1
SeGnPs		2.92	0.23	133	0.17	12.4	32.1

frequency could not be explained as Nernst diffusion in the pores of the electrode, which can also be characterized by a potential step chronoamperometry (CA; fig. S16).

In addition to the EIS analysis, cyclic voltammetry (CV) with different scan rates was carried out in both electrolytes (figs. S17 to S19). The remarkably higher anodic peak current (I_{pa}) and cathodic peak current (I_{pc}) observed for SeGnPs compared to Pt suggest higher electrocatalytic activity for the redox reaction of $Co(bpy)_3^{2+/3+}$ and I^-/I_3^-, which could be attributed to the lower R_{ct} at the SeGnP/electrolyte interface as observed in EIS measurements.

The electrochemical stability of CE materials is also one of the important factors that need to be considered for practical DSSC applications. On the basis of this consideration, the electrochemical stability of the SeGnPs was tested in both electrolytes (fig. S20). The reciprocal R_{ct} values of SeGnPs were nearly invariable after 1000 CV cycles in both electrolytes, whereas those of Pt decreased by less than 10% in both electrolytes at the final cycle (Fig. 2, C and D). SeGnPs displayed similar electrochemical stability even with a 1-month rest after 1000 CV measurements under normal laboratory conditions (fig. S21).

Theoretical calculations

We carried out DFT calculations for the CE/electrolyte interface to clarify the high electrocatalytic activity of SeGnPs for I_3^- reduction. The I_3^- reduction contains three elementary reaction steps

$$I_3^-(sol) \leftrightarrow I_2(sol) + I^-(sol) \quad (I)$$

$$I_2(sol) + 2^* \rightarrow 2I^* \quad (II)$$

$$I^* + e^- \rightarrow I^-(sol) \quad (III)$$

where the asterisk indicates the free site on the CE and "sol" indicates the electrolyte solvent. The solution reaction step I typically proceeds rapidly and in equilibrium, or the molecular iodine reduction reaction (IRR) steps II and III occurring at the CE/electrolyte interface are the rate-determining steps (*21*, *22*). Steps II and III in Pt occur rapidly and nearly simultaneously and induce the first of its two semicircles in the Nyquist plot (*21*, *22*). It has been recently shown that the adsorption

energy of I atom can serve as a good descriptor for the IRR. Specifically, it was argued that the adsorption energy should range between 0.33 and 1.20 eV, of which the former ensures the I_2 molecular dissociation and the latter desorption of I^- into I^- (sol) (*22*, *25*). Following the above-described experimental characterizations that have observed Se atoms only at the edges of GnPs, we set up SeGnP models based on the representative HGnP armchair and zigzag edges (Fig. 3A). Carefully treating the ferromagnetically spin-polarized graphene zigzag edge states (*26*, *27*), we performed DFT calculations to estimate the adsorption energies of atomic iodine under the vacuum and explicit acetonitrile solvation conditions (figs. S22 to S24) (*28*–*31*). For the pristine armchair and zigzag edges as well as the basal plane of GnPs, the I atom adsorption energies were determined to be below the optimal range for the CE catalytic activity (−0.17, 0.17, and −0.49 eV, respectively). Edge models involving double-coordinated Se (C–Se–C) or oxidized Se atoms were also unable to support stable I atom adsorption (Fig. 1A

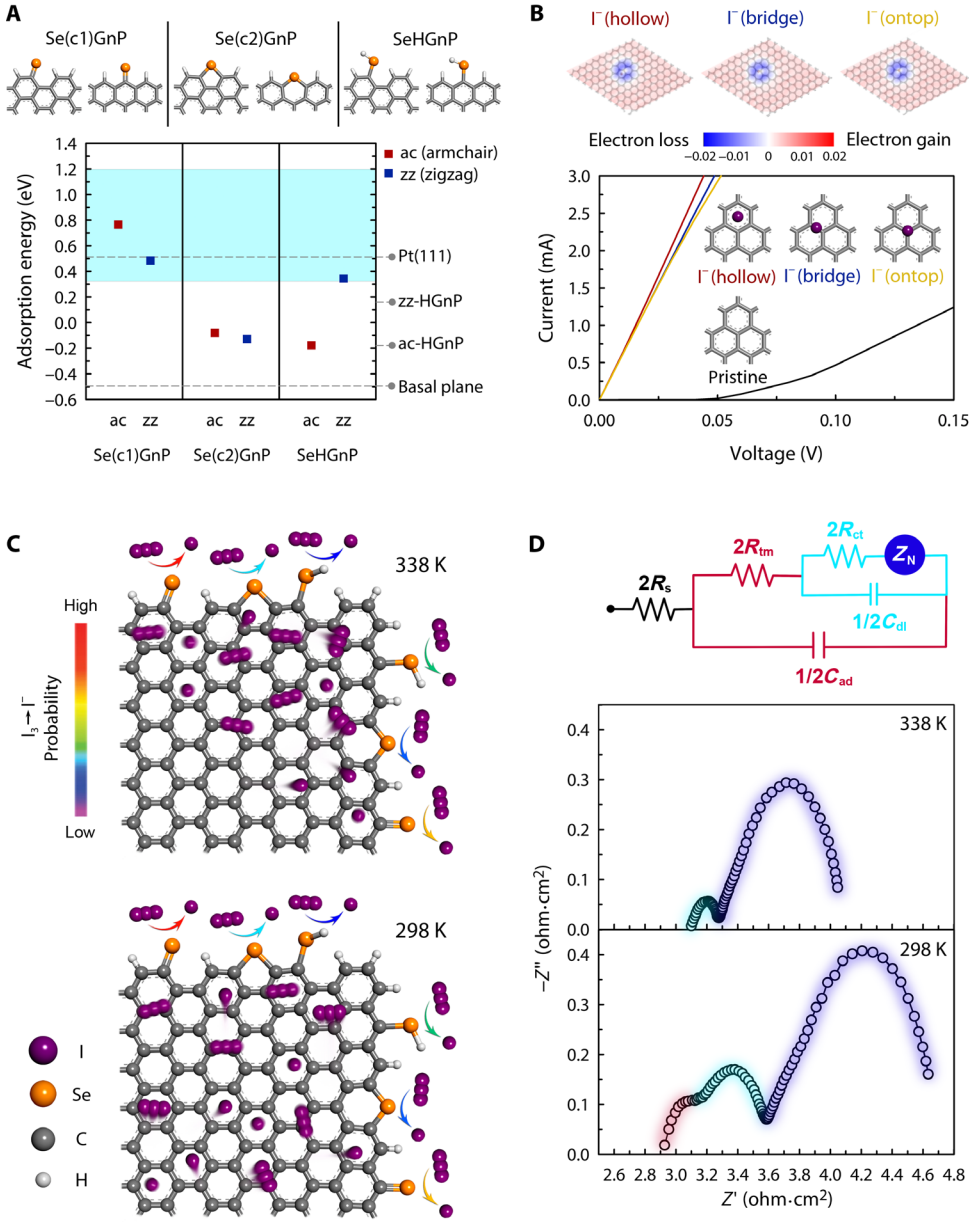

Fig. 3. Theoretical calculation and proposed mechanism of IRR. (**A**) For the representative single-coordinated, double-coordinated, and hydrogenated Se [Se(c1), Se(c2), and SeH, respectively]–doped armchair (ac) and zigzag (zz) graphene edges (top panel), the adsorption energies of the I atom explicitly solvated by acetonitrile molecules were evaluated and compared with the undoped edge and basal plane cases (bottom panel). The Pt(111) value of 0.52 eV has been taken from the study of Li *et al.* (*24*). In the bottom panel, the shaded region indicates the IRR activity criterion. (**B**) For various I^-- and I_3^--adsorbed graphene basal plane models (top panel and figs. S27 and S28), the current-voltage (*I-V*) curves were calculated and compared with those from pristine graphene (bottom panel). In the top panel, Mulliken charge populations were coded into atomic structures. (**C**) IRR mimetic diagram on the SeGnP surface. (**D**) Nyquist plots of SeGnP-CEs and their EC at room temperature.

and fig. S22). However, the I atom binding criterion was well satisfied for the single-coordinated Se-doping cases (C═Se), with adsorption energies of 0.77 and 0.48 eV for the armchair and zigzag edges, respectively.

We next theoretically investigate the origin of the first semicircle appearing in the Nyquist plot of the SeGnP-CEs in I^-/I_3^- electrolytes (Fig. 2B). As mentioned above, it is not fully understood why the EIS spectra of carbon-based materials, including HGnPs and SeGnPs, have three semicircles. Having identified the Se-doped graphitic edges as the primary sites where the I_3^- reduction takes place and as being responsible for the charge-transfer process that results in the second semicircle, we can assume that the first semicircle originates from the graphitic basal plane. To confirm this scenario, we carried out combined DFT (*29*, *32*–*34*) and NEGF calculations (*35*, *36*) and analyzed the structural, electronic, and charge transport properties of graphene adsorbed by I^-/I_3^- (figs. S25 and S26). The I_3^- and I^- ions were calculated to be adsorbed on the graphitic basal plane at the distances of 3.18 to 3.37 Å. This induces an n-type shift of the graphene band and significantly enhances the transmission or increases currents at finite bias voltages (Fig. 3B and fig. S28). The current increase has also been experimentally observed in CV measurements (figs. S18B and S19B), and we propose that although the graphitic basal plane cannot drive IRR by itself, its excellent current-carrying capability is a necessary condition to achieve the observed high CE catalytic activity. Extrapolation of the trend to the considerably larger $Co(bpy)_3^{2+/3+}$ electrolyte case also explains the absence of the first semicircle with $Co(bpy)_3^{2+/3+}$ (Fig. 2A). At high temperature, thermodynamic fluctuations of the I^-/I_3^- species and graphene would severely weaken the binding strength between the two and eventually initiate desorption of I^-/I_3^- from the graphitic basal plane. This explains the observation of the disappearance of the first semicircle at the high temperature limit (Fig. 3D and fig. S29).

The IRR mimetic diagram on the SeGnP surface, based on the electrochemical kinetics and DFT-NEGF results, is shown in Fig. 3C. The first semicircle is regarded as the transmission resistance (R_{tm}) and capacitance (C_{ad}) due to the adsorption of I^-/I_3^- on the graphitic basal plane, and the second semicircle is attributed to the R_{ct} and double-layer capacitance (C_{dl}) directly related to IRR activity at the Se-doped edge of the graphene and electrolyte interface. The third semicircle is the Nernst diffusion impedance (Z_N) of the redox couple between two electrodes. As a result, we can propose a new EC to elucidate the EIS spectrum of SeGnPs obtained from the IRR (Fig. 3D), with their EIS parameters summarized in Table 1. From the second semicircle of SeGnPs, the R_{ct} of SeGnPs (0.23 ohm·cm^2) was considerably lower than that of Pt (0.61 ohm·cm^2). From the first semicircles, the R_{tm} was 0.17 ohm·cm^2, and thus, the effective charge-transfer resistance ($\Re_{ct}$ = R_{tm} + R_{ct}) of SeGnPs is 0.40 ohm·cm^2, which is also lower than that of Pt. Thus, SeGnP-CEs are expected to exhibit a higher short-circuit current density (J_{sc}) and fill factor (FF) in DSSCs.

DSSC performance

Figure 4A shows the photocurrent-voltage (*J*-*V*) curves, with the photovoltaic parameters summarized in Table 2. The Pt-based DSSC with $Co(bpy)_3^{2+/3+}$ exhibited a J_{sc} of 15.30 mA cm^{-2}, an open-circuit voltage (V_{oc}) of 863 mV, an FF of 76.6%, and a PCE of 10.11%, whereas they were 16.27 mA cm^{-2}, 876 mV, 77.0%, and 10.98%, respectively, for the SeGnP-based DSSC. In the case of I^-/I_3^-, the Pt-based DSSC showed a J_{sc} of 17.26 mA cm^{-2}, a V_{oc} of 729 mV, an FF of 72.2%, and a PCE of 9.07%, whereas they were 18.16 mA cm^{-2}, 692 mV, 73.1%, and 9.17%,

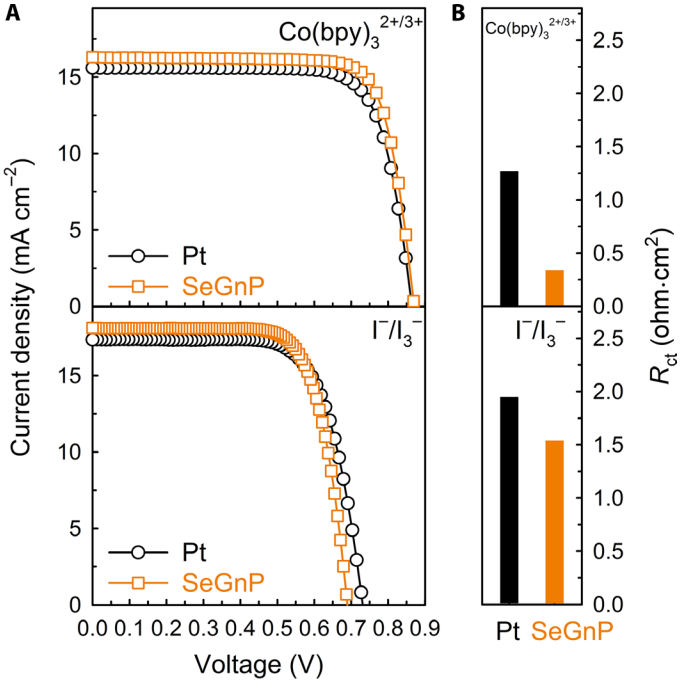

Fig. 4. DSSC performance of Pt-CEs and SeGnP-CEs. (**A**) *J*-*V* characteristics of the DSSCs with SM315/$Co(bpy)_3^{2+/3+}$ and N719/I^-/I_3^-. (**B**) R_{ct} of the same DSSCs.

respectively, for the SeGnP-based DSSC. Regardless of electrolytes, both the J_{sc} and FF values of SeGnP-based DSSCs are higher than those of their Pt-based counterparts.

DISCUSSION

This resulted in the net enhancement of the PCE, which was also confirmed with photocurrent transient dynamics and EIS measurements (fig. S30). The mass transport effect of the $Co(bpy)_3^{2+/3+}$ and I^-/I_3^- redox couples in actual DSSCs with different CEs was investigated by monitoring photocurrent transients using a multistep on/off modulation of the mass transfer limitation (fig. S30, A and B) (*37*, *38*). As can be seen, the ratio of the initial peak current to the steady-state current in the photocurrent transients is almost consistent in Pt-DSSCs and SeGnP-DSSCs with $Co(bpy)_3^{2+/3+}$, whereas Pt-DSSCs and SeGnP-DSSCs with I^-/I_3^- redox couple are significantly different. Considering that the DSSCs were fabricated under similar conditions, the mass transport of $Co(bpy)_3^{3+}$ and I_3^- ions in the pores of SeGnPs does not affect the overall cell efficiency.

To further understand the improved performance of the DSSCs with the SeGnP-CEs, EIS measurements were carried out on the DSSCs (fig. S30, C and D). The first semicircles of the DSSCs with the SeGnP-CEs are smaller than those of the Pt-CEs. From the first semicircles, the R_{ct} values calculated by using the EC (inset in fig. S30E) on the DSSC-SeGnP-CEs were 0.34 and 1.54 ohms·cm^2 for the $Co(bpy)_3^{2+/3+}$ and I^-/I_3^- redox couples, respectively, whereas the corresponding values of the DSSC-Pt-CEs were 1.27 and 1.95 ohms·cm^2. The lower R_{ct} values for the DSSCs with the SeGnP-CEs suggest higher electrocatalytic activities for the reduction of $Co(bpy)_3^{3+}$ and I_3^- ions than

Table 2. Photovoltaic performance of Pt-DSSCs and SeGnP-DSSCs with different electrolytes. J_{sc}, short-circuit current density; V_{oc}, open-circuit voltage.

CE	Dye	Electrolyte	J_{sc} (mA mA^{-2})	V_{oc} (mV)	FF (%)	PCE (%)
Pt	SM315	$Co(bpy)_3^{2+/3+}$	15.30 ± 0.36	863 ± 2.0	76.6 ± 0.4	10.11 ± 0.25
SeGnPs			16.27 ± 0.03	876 ± 6.5	77.0 ± 1.4	10.98 ± 0.17
Pt	N719	I^-/I_3^-	17.26 ± 0.32	729 ± 6.8	72.2 ± 1.1	9.07 ± 0.20
SeGnPs			18.16 ± 0.44	692 ± 2.9	73.1 ± 1.3	9.17 ± 0.04

the Pt counterparts, which could enhance the DSSC performance, in particular FF and J_{sc} (Table 2). The result is consistent with the feasibility of the heterogeneous electron-transfer process at the SeGnP/electrolyte interface, as indicated by the smaller R_{ct} (Fig. 4B).

In summary, we have proven SeGnPs to be Pt-free alternative CEs for the DSSCs in both $Co(bpy)_3^{2+/3+}$ and I^-/I_3^- electrolytes. Whereas carbon-based materials do not work properly for IRR, SeGnPs displayed unusual dual electrocatalytic activities with very high electrochemical stability in both electrolytes. Furthermore, the IRR mechanism, which has not been fully understood on carbon-based materials to date, was clarified by an electrochemical kinetics study combined with DFT and NEGF calculations. Se doping at the edges of GnPs, especially single-coordinated armchair and zigzag edges, was revealed as the source of the remarkably enhanced electrocatalytic activity. The well-preserved graphitic basal plane then rapidly transfers electrons from the external circuit to I_3^- ions at the edges, thus reducing the R_{ct} and hence improving the photovoltaic performance. On the basis of this new understanding, we proposed a new EC that should help in interpreting the IRR mechanism for other porous carbon-based materials such as heteroatom-doped graphene.

MATERIALS AND METHODS

Synthesis of SeGnPs

The SeGnPs were prepared simply by ball milling in a planetary ball mill capsule. Graphite (5.0 g) and Se (20.0 g) were placed into a stainless steel capsule containing stainless steel balls (500 g; diameter, 5 mm). After five charging/discharging cycles of argon under reduced pressure (0.05 mmHg), the capsule was sealed. Then, it was fixed in the planetary ball mill machine and agitated at 500 rpm for 48 hours. The resultant product was Soxhlet-extracted with CS_2 and further washed with 2.0 M aqueous KOH solution to remove unreacted Se and then repetitively extracted with 1 M aqueous HCl solution to get rid of remaining metallic impurities, if any. The final product was then freeze-dried at −120°C under a reduced pressure (0.05 mmHg) for 48 hours to yield 6.52 g (SeGnPs contained at least 1.52 g of Se) of dark black SeGnP powder.

Fabrication and characterization of DSSCs

FTO plates were cleaned in detergent solution, water, and ethanol using an ultrasonic bath. The FTO substrates were immersed in 40 mM aqueous $TiCl_4$ solution at 70°C for 30 min and washed with water and ethanol. A TiO_2 colloidal paste (18NR-T, Dyesol) was screen-printed onto FTO/glass and sintered at 500°C for 30 min in air. The thickness of the transparent layer was measured using an Alpha-step 250 surface profilometer (Tencor Instruments), and a paste for the scattering layer containing 500-nm-sized anatase particles (STP-500N, ENB Korea) was screen-printed and then dried for 2 hours at 25°C. The TiO_2 electrodes were sintered at 500°C for 30 min. The resulting TiO_2 photoanodes were immersed in a THF/ethanol (v/v, 2:1) solution containing 0.3 mM SM315 sensitizer (*39*) and 0.3 mM HC-A4 coadsorbent (or 0.3 mM N719 sensitizer only) (*40*) and kept at room temperature for 12 hours (see Supplementary Materials and Methods). The dye-adsorbed TiO_2 photoanodes were assembled with Pt-CEs and SeGnP-CEs using a thermal adhesive film (25-μm-thick Surlyn, DuPont) as a spacer to produce a sandwich-type cell. Electrolyte solution was introduced through a drilled hole on the CEs via vacuum backfilling. The hole was sealed with cover glass using Surlyn. The light intensity was adjusted with a Si solar cell that was doubled-checked with a National Renewable Energy Laboratory–calibrated Si solar cell (PV Measurement Inc.). The applied potential and cell current were measured using a Keithley digital source meter (model 2400). Photoelectrochemical data were measured using a 1000-W xenon light source (Oriel, 91193) that was focused to give 100 mW cm^{-2} (1 sun at AM 1.5 G). The *J-V* characteristics of the cell under these conditions were determined by externally biasing the cell and measuring the generated photocurrent. This process was fully automated using the WaveMetrics software. The measurement settling time between applying a voltage and measuring a current for the *J-V* characterization of DSSC was fixed to 80 ms.

DFT calculations

To determine the Se-doping geometries and iodine atom adsorption energies, we carried out DFT calculations using the VASP package (*28*) within the Perdew-Burke-Ernzerhof (PBE) parametrization of generalized gradient approximation (GGA) (*29*) augmented by DFT-D3 corrections (*30*). Valence electronic states were expanded in plane-wave basis sets with a 400-eV energy cutoff, and project-augmented wave method was used to represent core-valence electron interactions (*31*). All the structures were relaxed until the Hellmann-Feynman forces on each ion were less than 0.01 eV/Å. The vacuum distance between periodic images was modeled to have more than 16 Å. The single Γ-point in the Brillouin zone was sampled.

NEGF calculations

Electron transport properties were studied by conducting DFT-based NEGF calculations using the SIESTA-TranSIESTA package (*32*, *35*). For the initial DFT calculations, we used the PBE GGA (*29*) corrected by the DFT-D2 scheme (*33*). Core electrons were replaced by Troullier-Martins–type norm-conserving pseudopotentials (*34*), and the Kohn-Sham wave functions were expanded in terms of double-ζ plus polarization–level numerical atomic basis sets defined by a confinement energy of

100 meV. Real-space mesh corresponding to a cutoff energy of 200 rydbergs was used for grid operations, and a Monkhorst-Pack $2 \times 2 \times 1$ $\vec{k}$-point mesh was used to sample the Brillouin zone. For the subsequent NEGF calculations, we chose the charge transport direction along the armchair dimer lines, and starting from an orthogonal graphene cell composed of four C atoms, constructed a 5×12 supercell (5 dimer lines and 24 zigzag chains along the transport-normal and transport directions, respectively). The supercell was then divided into three equal-area regions, each of which was assigned as electrode 1, scattering region, or electrode 2. A fine $20 \times 1 \times 1$ Monkhorst-Pack grid was used for the $k_{\perp}$-point sampling along the transport-normal direction. To generate surface Green's functions, 15 $\vec{k}_{||}$ points along the transport direction were sampled for each electrode. In obtaining transmission functions, an energy grid from 2.0 eV below to 2.0 eV above the Fermi level was sampled at the 0.01-eV resolution. Using the transmission functions, the *I-V* characteristics were calculated according to the Landauer-Büttiker formula.

SUPPLEMENTARY MATERIALS

Supplementary material for this article is available at http://advances.sciencemag.org/cgi/content/full/2/6/e1501459/DC1

Supplementary Materials and Methods

fig. S1. Schematic representation of mechanochemical ball milling.

fig. S2. Field-emission SEM images and element mappings of SeGnPs.

fig. S3. Dark-field TEM image and element mappings with EDX (TEM) spectra.

fig. S4. EDX (SEM) and XPS spectra.

fig. S5. Nitrogen adsorption-desorption isotherms, Raman spectra, XRD patterns, and contact angles.

fig. S6. TGA thermograms.

fig. S7. Photographs of SeGnP dispersed solutions in various solvents.

fig. S8. AR-TEM, HR-TEM, and STEM images.

fig. S9. SEM images of SeGnP coated on FTO.

fig. S10. Schematic representation of symmetrical dummy cell and EC.

fig. S11. Electrocatalytic activities of the HGnP dummy cell in $Co(bpy)_3^{2+/3+}$ electrolytes.

fig. S12. Electrocatalytic activities of the reference HGnP dummy cell in I^-/I_3^- electrolytes.

fig. S13. EC model.

fig. S14. Optical transmittance, SEM images, and Nyquist plots.

fig. S15. Nyquist plots and resistance changes.

fig. S16. Potential step CA curves on symmetrical dummy cells.

fig. S17. Cyclic voltammograms in $Co(bpy)_3^{2+/3+}$ redox couple and oxidation and reduction peak.

fig. S18. Cyclic voltammograms in I^-/I_3^- redox couple and oxidation and reduction peak.

fig. S19. Cyclic voltammograms obtained at a scan rate of 50 mV s^{-1}.

fig. S20. Nyquist plots of the symmetrical dummy cells on $Co(bpy)_3^{2+/3+}$ and I^-/I_3^- electrolytes.

fig. S21. Nyquist plots measured 1 month later after 1000 cycling measurements.

fig. S22. Se-doped graphene models.

fig. S23. Adsorption geometries of the I atom on Se(c1)-GnP in vacuum and acetonitrile.

fig. S24. Se-doped models and the adsorption energies of the I atom.

fig. S25. Graphene models used in DFT and computational setup for NEGF.

fig. S26. Configurations of I^- or I_3^- adsorbed on graphene.

fig. S27. Mulliken charge populations.

fig. S28. Transmission functions of graphene and corresponding *I-V* characteristics.

fig. S29. Nyquist plots and R_{ct} and J_0 as temperature.

fig. S30. Photocurrent transient dynamics and Nyquist plots of DSSCs.

table S1. TGA, EA, EDX, and XPS data of the pristine graphite and SeGnPs.

table S2. BET surface area, pore volume, and pore size of the pristine graphite and SeGnPs.

table S3. The size of I_3^- and $Co(bpy)_3^{3+}$ ions.

References (*41–68*)

REFERENCES AND NOTES

1. B. O'Regan, M. Grätzel, A low-cost, high-efficiency solar cell based on dye-sensitized colloidal TiO_2 films. *Nature* **353**, 737–740 (1991).
2. J. E. Trancik, S. C. Barton, J. Hone, Transparent and catalytic carbon nanotube films. *Nano Lett.* **8**, 982–987 (2008).
3. J. Han, H. Kim, D. Y. Kim, S. M. Jo, S.-Y. Jang, Water-soluble polyelectrolyte-grafted multiwalled carbon nanotube thin films for efficient counter electrode of dye-sensitized solar cells. *ACS Nano* **4**, 3503–3509 (2010).
4. B. Fang, S.-Q. Fan, J. H. Kim, M.-S. Kim, M. Kim, N. K. Chaudhari, J. Ko, J.-S. Yu, Incorporating hierarchical nanostructured carbon counter electrode into metal-free organic dye-sensitized solar cell. *Langmuir* **26**, 11238–11243 (2010).
5. G. Wang, C. Huang, W. Xing, S. Zhuo, Micro–meso hierarchical porous carbon as low-cost counter electrode for dye-sensitized solar cells. *Electrochim. Acta* **56**, 5459–5463 (2011).
6. D.-S. Yang, C. Kim, M. Y. Song, H.-Y. Park, J. C. Kim, J.-J. Lee, M. J. Ju, J.-S. Yu, N-doped hierarchical hollow mesoporous carbon as metal-free cathode for dye-sensitized solar cells. *J. Phys. Chem. C* **118**, 16694–16702 (2014).
7. Z. Huang, X. Liu, K. Li, D. Li, Y. Luo, H. Li, W. Song, L. Chen, Q. Meng, Application of carbon materials as counter electrodes of dye-sensitized solar cells. *Electrochem. Commun.* **9**, 596–598 (2007).
8. K. Imoto, K. Takahashi, T. Yamaguchi, T. Komura, J.-i. Nakamura, K. Murata, High-performance carbon counter electrode for dye-sensitized solar cells. *Sol. Energy Mater. Sol. Cells* **79**, 459–469 (2003).
9. Y. Xue, J. Liu, H. Chen, R. Wang, D. Li, J. Qu, L. Dai, Nitrogen-doped graphene foams as metal-free counter electrodes in high-performance dye-sensitized solar cells. *Angew. Chem. Int. Ed.* **51**, 12124–12127 (2012).
10. M. J. Ju, J. C. Kim, H.-J. Choi, I. T. Choi, S. G. Kim, K. Lim, J. Ko, J.-J. Lee, I.-Y. Jeon, J.-B. Baek, H. K. Kim, N-Doped graphene nanoplatelets as superior metal-free counter electrodes for organic dye-sensitized solar cells. *ACS Nano* **7**, 5243–5250 (2013).
11. I.-Y. Jeon, H.-J. Choi, M. J. Ju, I. T. Choi, K. Lim, J. Ko, H. K. Kim, J. C. Kim, J.-J. Lee, D. Shin, S.-M. Jung, J.-M. Seo, M.-J. Kim, N. Park, L. Dai, J.-B. Baek, Direct nitrogen fixation at the edges of graphene nanoplatelets as efficient electrocatalysts for energy conversion. *Sci. Rep.* **3**, 2260 (2013).
12. M. J. Ju, I.-Y. Jeon, J. C. Kim, K. Lim, H.-J. Choi, S.-M. Jung, I. T. Choi, Y. K. Eom, Y. J. Kwon, J. Ko, J.-J. Lee, H. K. Kim, J.-B. Baek, Graphene nanoplatelets doped with N at its edges as metal-free cathodes for organic dye-sensitized solar cells. *Adv. Mater.* **26**, 3055–3062 (2014).
13. M. J. Ju, I.-Y. Jeon, K. Lim, J. C. Kim, H.-J. Choi, I. T. Choi, Y. K. Eom, Y. J. Kwon, J. Ko, J.-J. Lee, J.-B. Baek, H. K. Kim, Edge-carboxylated graphene nanoplatelets as oxygen-rich metal-free cathodes for organic dye-sensitized solar cells. *Energy Environ. Sci.* **7**, 1044–1052 (2014).
14. J. D. Roy-Mayhew, D. J. Bozym, C. Punckt, I. A. Aksay, Functionalized graphene as a catalytic counter electrode in dye-sensitized solar cells. *ACS Nano* **4**, 6203–6211 (2010).
15. L. Kavan, J.-H. Yum, M. Grätzel, Graphene nanoplatelets outperforming platinum as the electrocatalyst in co-bipyridine-mediated dye-sensitized solar cells. *Nano Lett.* **11**, 5501–5506 (2011).
16. S. Hou, X. Cai, H. Wu, X. Yu, M. Peng, K. Yan, D. Zou, Nitrogen-doped graphene for dye-sensitized solar cells and the role of nitrogen states in triiodide reduction. *Energy Environ. Sci.* **6**, 3356–3362 (2013).
17. S. Ahmad, J.-H. Yum, H.-J. Butt, M. K. Nazeeruddin, M. Grätzel, Efficient platinum-free counter electrodes for dye-sensitized solar cell applications. *ChemPhysChem* **11**, 2814–2819 (2010).
18. Q. Li, J. Wu, Q. Tang, Z. Lan, P. Li, J. Lin, L. Fan, Application of microporous polyaniline counter electrode for dye-sensitized solar cells. *Electrochem. Commun.* **10**, 1299–1302 (2008).
19. M. Wang, A. M. Anghel, B. Marsan, N.-L. Cevey Ha, N. Pootrakulchote, S. M. Zakeeruddin, M. Grätzel, CoS supersedes Pt as efficient electrocatalyst for triiodide reduction in dye-sensitized solar cells. *J. Am. Chem. Soc.* **131**, 15976–15977 (2009).
20. I.-Y. Jeon, Y.-R. Shin, G.-J. Sohn, H.-J. Choi, S.-Y. Bae, J. Mahmood, S.-M. Jung, J.-M. Seo, M.-J. Kim, D. W. Chang, L. Dai, J.-B. Baek, Edge-carboxylated graphene nanosheets via ball milling. *Proc. Natl. Acad. Sci. U.S.A.* **109**, 5588–5593 (2012).
21. A. Hauch, A. Georg, Diffusion in the electrolyte and charge-transfer reaction at the platinum electrode in dye-sensitized solar cells. *Electrochim. Acta* **46**, 3457–3466 (2001).
22. Y. Hou, D. Wang, X. H. Yang, W. Q. Fang, B. Zhang, H. F. Wang, G. Z. Lu, P. Hu, H. J. Zhao, H. G. Yang, Rational screening low-cost counter electrodes for dye-sensitized solar cells. *Nat. Commun.* **4**, 1583 (2013).
23. W. Kwon, J.-M. Kim, S.-W. Rhee, A new equivalent circuit model for porous carbon electrodes in charge transfer reaction of iodide/triiodide redox couples. *Electrochim. Acta* **68**, 110–113 (2012).
24. G. R. Li, J. Song, G. L. Pan, X. P. Gao, Highly Pt-like electrocatalytic activity of transition metal nitrides for dye-sensitized solar cells. *Energy Environ. Sci.* **4**, 1680–1683 (2011).
25. B. Zhang, D. Wang, Y. Hou, S. Yang, X. H. Yang, J. H. Zhong, J. Liu, H. F. Wang, P. Hu, H. J. Zhao, H. G. Yang, Facet-dependent catalytic activity of platinum nanocrystals for triiodide reduction in dye-sensitized solar cells. *Sci. Rep.* **3**, 1836 (2013).
26. M. Fujita, K. Wakabayashi, K. Nakada, K. Kusakabe, Peculiar localized state at zigzag graphite edge. *J. Phys. Soc. Jpn.* **65**, 1920–1923 (1996).
27. H. Lee, Y.-W. Son, N. Park, S. Han, J. Yu, Magnetic ordering at the edges of graphitic fragments: Magnetic tail interactions between the edge-localized states. *Phys. Rev. B* **72**, 174431 (2005).

28. G. Kresse, J. Furthmüller, Efficient iterative schemes for ab initio total-energy calculations using a plane-wave basis set. *Phys. Rev. B* **54**, 11169–11186 (1996).
29. J. P. Perdew, K. Burke, M. Ernzerhof, Generalized gradient approximation made simple. *Phys. Rev. Lett.* **77**, 3865–3868 (1996).
30. S. Grimme, J. Antony, S. Ehrlich, S. Krieg, A consistent and accurate ab initio parametrization of density functional dispersion correction (DFT-D) for the 94 elements H-Pu. *J. Chem. Phys.* **132**, 154104 (2010).
31. P. E. Blöchl, Projector augmented-wave method. *Phys. Rev. B* **50**, 17953–17979 (1994).
32. J. M. Soler, E. Artacho, J. D. Gale, A. García, J. Junquera, P. Ordejón, D. Sánchez-Portal, The SIESTA method for ab initio order-*N* materials simulation. *J. Phys. Condens. Matter* **14**, 2745–2779 (2002).
33. S. Grimme, Semiempirical GGA-type density functional constructed with a long-range dispersion correction. *J. Comput. Chem.* **27**, 1787–1799 (2006).
34. N. Troullier, J. L. Martins, Efficient pseudopotentials for plane-wave calculations. *Phys. Rev. B* **43**, 1993–2006 (1991).
35. M. Brandbyge, J. L. Mozos, P. Ordejón, J. Taylor, K. Stokbro, Density-functional method for nonequilibrium electron transport. *Phys. Rev. B* **65**, 165401 (2002).
36. Y.-H. Kim, J. Tahir-Kheli, P. A. Schultz, W. A. Goddard III, First-principles approach to the charge-transport characteristics of monolayer molecular-electronics devices: Application to hexanedithiolate devices. *Phys. Rev. B* **73**, 235419 (2006).
37. S. M. Feldt, E. A. Gibson, E. Gabrielsson, L. Sun, G. Boschloo, A. Hagfeldt, Design of organic dyes and cobalt polypyridine redox mediators for high-efficiency dye-sensitized solar cells. *J. Am. Chem. Soc.* **132**, 16714–16724 (2010).
38. A. Yella, H.-W. Lee, H. N. Tsao, C. Yi, A. K. Chandiran, M. K. Nazeeruddin, E. W.-G. Diau, C.-Y. Yeh, S. M. Zakeeruddin, M. Grätzel, Porphyrin-sensitized solar cells with cobalt (II/III)–based redox electrolyte exceed 12 percent efficiency. *Science* **334**, 629–634 (2011).
39. S. Mathew, A. Yella, P. Gao, R. Humphry-Baker, B. F. E. Curchod, N. Ashari-Astani, I. Tavernelli, U. Rothlisberger, M. K. Nazeeruddin, M. Grätzel, Dye-sensitized solar cells with 13% efficiency achieved through the molecular engineering of porphyrin sensitizers. *Nat. Chem.* **6**, 242–247 (2014).
40. I. T. Choi, B. S. You, Y. K. Eom, M. J. Ju, W. S. Choi, S. H. Kang, M. S. Kang, K. D. Seo, J. Y. Hong, S. H. Song, J.-W. Yang, H. K. Kim, Triarylamine-based dual-function coadsorbents with extended π-conjugation aryl linkers for organic dye-sensitized solar cells. *Org. Electron.* **15**, 3316–3326 (2014).
41. H. N. Tsao, C. Yi, T. Moehl, J.-H. Yum, S. M. Zakeeruddin, M. K. Nazeeruddin, M. Grätzel, Cyclopentadithiophene bridged donor–acceptor dyes achieve high power conversion efficiencies in dye-sensitized solar cells based on the tris-cobalt bipyridine redox couple. *ChemSusChem* **4**, 591–594 (2011).
42. J. C. Slater, Atomic radii in crystals. *J. Chem. Phys.* **41**, 3199–3204 (1964).
43. A. Allouche, Y. Ferro, Dissociative adsorption of small molecules at vacancies on the graphite (0 0 0 1) surface. *Carbon* **44**, 3320–3327 (2006).
44. G. Zorn, S. R. Dave, X. Gao, D. G. Castner, Method for determining the elemental composition and distribution in semiconductor core–shell quantum dots. *Anal. Chem.* **83**, 866–873 (2011).
45. A. Diener, T. Neumann, U. Kramar, D. Schild, Structure of selenium incorporated in pyrite and mackinawite as determined by XAFS analyses. *J. Contam. Hydrol.* **133**, 30–39 (2012).
46. P. V. Galiy, A. V. Musyanovych, Ya. M. Fiyala, The interface microscopy and spectroscopy on the cleavage surfaces of the In_4Se_3 pure and copper-intercalated layered crystals. *Physica E* **35**, 88–92 (2006).
47. K. Han, Z. Liu, H. Ye, F. Dai, Flexible self-standing graphene–Se@CNT composite film as a binder-free cathode for rechargeable Li–Se batteries. *J. Power Sources* **263**, 85–89 (2014).
48. M. V. Andreocci, C. Furlani, G. Mattogno, R. Zanoni, F. A. Devillanova, G. Verani, An XPS investigation on some selenium-containing ligands: Azolidine derivatives. *Inorg. Chim. Acta* **51**, 98–101 (1981).
49. Z. Ryu, J. Zheng, M. Wang, B. Zhang, Characterization of pore size distributions on carbonaceous adsorbents by DFT. *Carbon* **37**, 1257–1264 (1999).
50. K. N. Kudin, B. Ozbas, H. C. Schniepp, R. K. Prud'homme, I. A. Aksay, R. Car, Raman spectra of graphite oxide and functionalized graphene sheets. *Nano Lett.* **8**, 36–41 (2008).
51. Y. Wen, K. He, Y. Zhu, F. Han, Y. Xu, I. Matsuda, Y. Ishii, J. Cumings, C. Wang, Expanded graphite as superior anode for sodium-ion batteries. *Nat. Commun.* **5**, 4033 (2014).
52. K. Singh, A. Ohlan, V. H. Pham, B. R., S. Varshney, J. Jang, S. H. Hur, W. M. Choi, M. Kumar, S. K. Dhawan, B.-S. Kong, J. S. Chung, Nanostructured graphene/Fe_3O_4 incorporated polyaniline as a high performance shield against electromagnetic pollution. *Nanoscale* **5**, 2411–2420 (2013).
53. O. E. D. Rodrigues, G. D. Saraiva, R. O. Nascimento, E. B. Barros, J. Mendes Filho, Y. A. Kim, H. Muramatsu, M. Endo, M. Terrones, M. S. Dresselhaus, A. G. Souza Filho, Synthesis and characterization of selenium–carbon nanocables. *Nano Lett.* **8**, 3651–3655 (2008).
54. M. de Selincourt, The boiling point of selenium. *Proc. Phys. Soc.* **52**, 348 (1940).
55. H. A. Becerril, J. Mao, Z. Liu, R. M. Stoltenberg, Z. Bao, Y. Chen, Evaluation of solution-processed reduced graphene oxide films as transparent conductors. *ACS Nano* **2**, 463–470 (2008).
56. A. Hagfeldt, G. Boschloo, L. Sun, L. Kloo, H. Pettersson, Dye-sensitized solar cells. *Chem. Rev.* **110**, 6595–6663 (2010).
57. J.-M. Kim, S.-W. Rhee, Electrochemical properties of porous carbon black layer as an electron injector into iodide redox couple. *Electrochim. Acta* **83**, 264–270 (2012).
58. Y. Y. Dou, G. R. Li, J. Song, X. P. Gao, Nickel phosphide-embedded graphene as counter electrode for dye-sensitized solar cells. *Phys. Chem. Chem. Phys.* **14**, 1339–1342 (2012).
59. L. Kavan, J.-H. Yum, M. Grätzel, Graphene-based cathodes for liquid-junction dye sensitized solar cells: Electrocatalytic and mass transport effects. *Electrochim. Acta* **128**, 349–359 (2014).
60. H. N. Tsao, P. Comte, C. Yi, M. Grätzel, Avoiding diffusion limitations in cobalt(III/II)-tris(2,2′-bipyridine)-based dye-sensitized solar cells by tuning the mesoporous TiO_2 film properties. *ChemPhysChem* **13**, 2976–2981 (2012).
61. C.-L. Chen, H. Teng, Y.-L. Lee, In situ gelation of electrolytes for highly efficient gel-state dye-sensitized solar cells. *Adv. Mater.* **23**, 4199–4204 (2011).
62. A. J. Bard, L. R. Faulkner, *Electrochemical Methods: Fundamentals and Applications* (Wiley, New York, 1980), vol. 2.
63. C.-I. Chia, V. H. Crespi, Stabilizing the zigzag edge: Graphene nanoribbons with sterically constrained terminations. *Phys. Rev. Lett.* **109**, 076802 (2012).
64. F. Cervantes-Sodi, G. Csányi, S. Piscanec, A. C. Ferrari, Edge-functionalized and substitutionally doped graphene nanoribbons: Electronic and spin properties. *Phys. Rev. B* **77**, 165427 (2008).
65. G. Lee, K. Cho, Electronic structures of zigzag graphene nanoribbons with edge hydrogenation and oxidation. *Phys. Rev. B* **79**, 165440 (2009).
66. E. Cruz-Silva, Z. M. Barnett, B. G. Sumpter, V. Meunier, Structural, magnetic, and transport properties of substitutionally doped graphene nanoribbons from first principles. *Phys. Rev. B* **83**, 155445 (2011).
67. S. S. Kim, H. S. Kim, H. S. Kim, Y.-H. Kim, Conductance recovery and spin polarization in boron and nitrogen co-doped graphene nanoribbons. *Carbon* **81**, 339–346 (2015).
68. G. Makov, M. C. Payne, Periodic boundary conditions in ab initio calculations. *Phys. Rev. B* **51**, 4014–4022 (1995).

Acknowledgments

Funding: J.-B.B. was supported by Creative Research Initiative (2014R1A3A2069102) and BK21 PLUS (Brain Korea 21 Program for Leading Universities & Students) programs (10Z20130011057) through the National Research Foundation (NRF) of Korea. Y.-H.K. was supported by NRF Global Frontier Hybrid Interface Materials program (2013M3A6B1078881). H.K.K. would like to acknowledge NRF grant 2014R1A2A1A10051630. **Author contributions:** J.-B.B. conceived SeGnPs and oversaw all the research phases. I.-Y.J. and J.-B.B. designed the experiments and interpreted the data. I.-Y.J., S.-M.J., and J.-M.S. conducted the syntheses and characterizations. M.J.J. conceived and oversaw the electrochemical and solar cell study. H.M.K., I.T.C., S.H.K., J.-J.L., and H.K.K. conducted the electrochemical and solar cell study. Y.-H.K. designed and oversaw the computational research. J.I.C. performed DFT calculations, and H.S.K. and M.J.N. carried out NEGF calculations. H.Y.J. was involved in the AR-TEM experiments. J.-B.B., Y.-H.K., M.J.J., and I.-Y.J. wrote the paper and discussed the results. All authors contributed to and commented on this article. **Competing interests:** The authors declare that they have no competing interests. **Data and materials availability:** All data needed to evaluate the conclusions in the paper are present in the paper and/or the Supplementary Materials. Additional data related to this paper may be requested from the authors.

Submitted 14 October 2015
Accepted 23 May 2016
Published 17 June 2016
10.1126/sciadv.1501459

Citation: M. J. Ju, I.-Y. Jeon, H. M. Kim, J. I. Choi, S.-M. Jung, J.-M. Seo, I. T. Choi, S. H. Kang, H. S. Kim, M. J. Noh, J.-J. Lee, H. Y. Jeong, H. K. Kim, Y.-H. Kim, J.-B. Baek, Edge-selenated graphene nanoplatelets as durable metal-free catalysts for iodine reduction reaction in dye-sensitized solar cells. *Sci. Adv.* **56**, e1501459 (2016).

Edge-selenated graphene nanoplatelets as durable metal-free catalysts for iodine reduction reaction in dye-sensitized solar cells

Myung Jong Ju, In-Yup Jeon, Hong Mo Kim, Ji Il Choi, Sun-Min Jung, Jeong-Min Seo, In Taek Choi, Sung Ho Kang, Han Seul Kim, Min Jong Noh, Jae-Joon Lee, Hu Young Jeong, Hwan Kyu Kim, Yong-Hoon Kim and Jong-Beom Baek (June 17, 2016)

Sci Adv 2016, 2:.
doi: 10.1126/sciadv.1501459